In situ structural determination of *3d* and *5d* perovskite oxides under high pressure by synchrotron x-ray diffraction

Jie Chen [1], Jiaming He,[1] Yanyao Zhang [2], Stella Chariton [3], Vitali Prakapenka [3], Kazunari Yamaura [4,5], Jung-Fu Lin [2],
J. B. Goodenough,[1] and J.-S. Zhou [1,*]

[1]*Materials Science and Engineering Program, Mechanical Engineering, University of Texas at Austin, Austin, Texas 78712, USA*
[2]*Department of Earth and Planetary Sciences, Jackson School of Geosciences, The University of Texas at Austin, Austin, Texas 78712, USA*
[3]*Center for Advanced Radiation Sources, The University of Chicago, Illinois 60637, USA*
[4]*Research Center for Materials Nanoarchitectonics (MANA),*
National Institute for Materials Science, 1-1 Namiki, Tsukuba, Ibaraki 305-0044, Japan
[5]*Graduate School of Chemical Sciences and Engineering,*
Hokkaido University, North 10 West 8, Kita-ku, Sapporo, Hokkaido 060–0810, Japan

In contrast to the Mott transition found in RNiO$_3$ ($R=$ rare earths), the metal-insulator transition temperature in the perovskite NaOsO$_3$ is not sensitive to pressure. The peculiarity may be correlated to how the crystal structure of NaOsO$_3$ responds to high pressure, which has been rarely studied so far. The pressure-induced bond-length shrinking can increase the orbital overlap integral and therefore the electron bandwidth. However, in the orthorhombic perovskite structure, the pressure-induced bending in the bond angle Os-O-Os may compensate for the bandwidth broadening due to the bond-length shrinking in some circumstances. A recent structural study on polycrystalline NaOsO$_3$ indicated that orthorhombic distortion is enlarged under high pressure. But, how the local structure changes under pressure remains unknown. Moreover, a highly unusual phase transition from the orthorhombic phase (*Pbnm*) to a polar phase (*Pbn*2$_1$) occurs at around 18 GPa [Sereika *et al.*, npj Quantum Mater. **5**, 66 (2020)]. Motivated by these concerns, we have done a more comprehensive structural study on NaOsO$_3$ using single-crystal diffraction with synchrotron radiation at high pressures up to 41 GPa. Diffraction patterns over the entire pressure range can be refined well with the *Pbnm* structural model. Moreover, the refinement results reveal in detail how the local structures change under pressure corresponding to the enhanced orthorhombic distortion from the lattice parameters. We have carried out a systematic study for understanding the pressure effect on the orthorhombic perovskites in the context of the influences of the charge distributions in the ABO$_3$ formula, i.e., $A^{3+}B^{3+}$O$_3$, $A^{2+}B^{4+}$O$_3$, and $A^{1+}B^{5+}$O$_3$ and the B-site cations from the 3d to the 4d and 5d row of elements. To fulfill this purpose, we have revisited two families of 3d perovskites: RCrO$_3$ and RFeO$_3$.

I. INTRODUCTION

The complex osmate oxides A^{1+}Os^{5+}O$_3$ have attracted much attention over the past decade due to their intriguing physical properties. The rhombohedral LiNbO$_3$-type (LNO) LiOsO$_3$ undergoes a transition from a nonpolar phase (*R-3c*) to a polar phase (*R3c*) at 130 K, while it is metallic down to the lowest temperature [1]. This finding contradicts the common belief that most ferroelectrics are insulators. By substituting an even larger Na$^+$ for Li$^+$ in A^+Os^{5+}O$_3$, an orthorhombic perovskite NaOsO$_3$ is stabilized. A metal-insulator transition (MIT) accompanied with a G-type antiferromagnetic ordering occurs in NaOsO$_3$ at 410 K. The origin of this MIT is still under debate. As there is no abrupt volume change on crossing the transition, the phase transition has been believed to be driven by the magnetic ordering, as proposed by Slater in 1951 [2]. However, critical fluctuations revealed by a resonant inelastic x ray scattering (RIXS) experiment imply that the

Mott physics still plays a significant role in the transition of NaOsO$_3$ [3]. High pressure can be used to increase the bandwidth of materials by reducing the cell volume. Surprisingly, the T_{MIT} of NaOsO$_3$ decreases slightly under pressure as observed from the resistivity measurements [4]. This is in sharp contrast to the giant pressure effect on T_{MIT} in the Mott insulators RNiO$_3$ [5–8]. The difference of pressure dependence of transition temperatures may lie in how the crystal structure responds to high pressure in the 3d and 5d perovskites.

Sereika *et al.* have studied the crystal structure of NaOsO$_3$ under high pressure using synchrotron x-ray powder diffraction [4]. They found that although the orthorhombic distortion is significantly enlarged under pressure, the *Pbnm* phase remains stable up to 18 GPa. Above 18 GPa, the diffraction patterns can be refined with a polar-phase model (*Pbn*2$_1$). The pressure-induced phase transition to a polar phase in the perovskite NaOsO$_3$ contradicts the observations in the popular ferroelectric perovskites where pressure favors the nonpolar phase. [9–11] However, there are rare examples where pressure favors the polar phase, as seen in LiOsO$_3$ and a Pb-based perovskite oxide. In LiOsO$_3$, the transition temperature to the

*jszhou@mail.utexas.edu
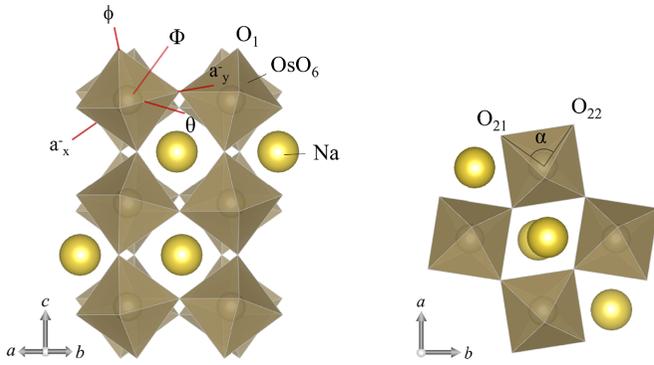
FIG. 1. Structural model of *Pbnm* perovskite.

polar phase ($R3c$) increases drastically under pressure, as seen from the measurement of resistivity and the *in situ* studies of Raman and x-ray diffraction [12,13]. The pressure creates some structural instability by raising the bond-valence sum (BVS) in the LiO_9 polyhedra. The displacement of Li^+ to break the inversion symmetry takes place for reducing the unusually high BVS [13]. In another example, the strong hybridization between the lone-pair electrons on Pb^{2+} and the Ru t_{2g} orbitals enabled under pressure leads to a phase transition to the polar phase ($Pbn2_1$) at 32 GPa, in which the Pb-Ru distance becomes unprecedentedly short among perovskite oxides [14]. Therefore, it is important to determine the local structural changes in the perovskite $NaOsO_3$ under pressure to understand the possibility of this unusual phase transition. Additionally, the possible phase transition can be verified conclusively by single-crystal diffraction because the technique is more sensitive to the symmetry change.

The orthorhombic perovskite structure is the most popular structure within the ABO_3 perovskite family. The *Pbnm* space group allows the cooperative octahedral-site rotations, the bond-length splitting in BO_6 octahedra, and the dislocation of the A-site cations from the position in the cubic perovskite structure as illustrated in Fig. 1. Physical properties in the orthorhombic perovskites are highly sensitive to the local structural distortions. For example, the spin-state transition in $RCoO_3$, the metal-insulator transition in $RNiO_3$, and the orbital ordering and flipping transitions in RVO_3 are closely correlated to the local structural distortions [15–19]. The physical properties can also be tuned by applying high pressure [5–8,20–25]. However, the knowledge of how the orthorhombic crystal structure responds to high pressure remains incomplete. The high-pressure structural study of the orthorhombic perovskites is also of interest in geosciences since the perovskite is the major form of matter in the earth's mantle.

The degree of orthorhombic structural distortions in the perovskite is closely related to the geometric tolerance factor t, which is defined as

$$t = (A\text{-}O)/\sqrt{2}(B\text{-}O), \qquad (1)$$

where A-O and B-O are the equilibrium bond length. The pressure-induced structural distortions can be determined by the dependence of the t factor under pressure, dt/dP. However, the prediction of the structural behavior under pressure requires the structural data from a high, precise structural

study under pressure. Zhao *et al.* [26] have shown that the ratio of the site compressibility is inversely proportional to the ratio of the site bond-valence sum. Therefore, one can predict the structural behavior under pressure based on the structural data at ambient pressure. Based on this relationship, the authors predicted a $dt/dP > 0$ for the orthorhombic perovskites $A^{3+}B^{3+}O_3$ and a $dt/dP < 0$ for the $A^{2+}B^{4+}O_3$ perovskites. While the $A^{2+}B^{4+}O_3$ perovskites show an overwhelming negative dt/dP [26–29], both positive and negative dt/dP can be found in many cases of $A^{3+}B^{3+}O_3$ perovskites.

Zhou [30] has argued that the sign of dt/dP depends on the local structural distortions at ambient pressure in the $A^{3+}B^{3+}O_3$ perovskites. A $dt/dP < 0$ occurs in the perovskites with a t factor in the low end of the group, whereas a $dt/dP > 0$ holds in those with a t factor in the high end of the group. However, the very small magnitude of dt/dP for the case of $dt/dP < 0$ leaves some uncertainty in identifying the sign change by the structural study under pressure with the laboratory x ray. This work aims to confirm the unambiguous sign change of dt/dP in two perovskite families, $R^{3+}Fe^{3+}O_3$ and $R^{3+}Cr^{3+}O_3$ using synchrotron x-ray diffraction.

II. EXPERIMENT

A. Sample synthesis

Single-crystal $NaOsO_3$ was synthesized under high-pressure and high-temperature conditions by solid-state reaction. The starting materials Na_2O_2 (97%, Sigma-Aldrich), OsO_2 [laboratory made from 99.95% Os (Nanjing Dongrui Platinum Co., Ltd.)], and NaCl (99.99%, Rare Metallic Co.) at a molar ratio of $Na_2O_2 : OsO_2:NaCl = 0.6:1:0.1$ were thoroughly mixed and then sealed in a Pt capsule. The procedure was conducted in an Ar-filled glovebox. Under a pressure of 6 GPa produced by a multianvil-type apparatus, the assembly was heated at 1500 °C for 1 hour and quenched to room temperature before releasing the pressure. The obtained crystals were dark purple in color. The selected crystal flakes for the *in situ* single-crystal x-ray diffraction (XRD) and Raman measurements were polished on double sides down to $\sim$ 7-μm thickness by using diamond films.

B. The crystal preparation, diamond-anvil cell, and single-crystal x-ray diffraction with synchrotron radiation

Three $NaOsO_3$ crystal flakes were loaded into a short-symmetric diamond-anvil cell (DAC) with a pair of diamond anvils mounted on tungsten carbide seats with a large aperture of around 80°. The culet size of the diamond anvils was 200 μm. The thickness of the rhenium gasket was preindented to around 24 μm and a 120-μm-diameter hole was drilled in the center as the sample chamber. A pressed pellet with 2-μm thickness of polycrystalline Pt and a chip of ruby as the pressure manometer were placed in the center and the edge of the gasket hole. Neon gas was used as the pressure medium. The image of the crystal flakes in the pressure chamber is shown in Fig. S1 in Supplemental Material [31].

Single-crystal diffraction under pressure were conducted at 13ID-D beamline of the GeoSoiEnviroCARS, Advanced Photon Source, Argonne National Laboratory. The wavelength of the x-ray beam was 0.2952 Å and the beam could focus on a

$\sim 3 \times 3$-μm^2 area. The sample stage was rotated over $\pm 29°$ along the vertical axis of the DAC during data collections. A typical pattern of single-crystal diffraction is displayed in Fig. S1 [31]. The chamber pressure was checked before and after each pressure point from the XRD of Pt [32].

C. The structure refinement

The CRYSALIS PRO software has been used to determine the unit cell and lattice parameters, followed by extracting intensity for *hkl* reflections and performing absorption correction. Structure refinements have been conducted by JANA 2006 software [33].

For the reason discussed in the text, the refinements in the pressure range from 20 to 30 GPa are not converged. In this case, the x-ray powder-diffraction patterns converted from single-crystal XRD by DIOPTAS software were analyzed by the Le Bail profile fitting method by using RIETAN-FP and VESTA software [34,35].

D. Powder diffraction and refinement

Power diffraction of RCrO$_3$ and RFeO$_3$ with DAC was done at the 13-ID-D beamline of the GSECARS, Advanced Photon Source, Argonne National Laboratory. Powder sample of RCrO$_3$ and RFeO$_3$ were obtained by solid-state reaction or pulverization of single-crystal samples. The grain size of the powder was crucial in avoiding preferred orientation. By evaporating the liquid with suspended particles, the samples with fine particle size were prepared for the structural study. The powder was pressed into small pellets and loaded into a DAC along with Au as the initial pressure indicator. Neon was used as the pressure medium. The culet size of the diamond anvil was 300 μm. Pressure was read before and after each measurement. The sample stage was rotated slightly $\pm 5°$ during the measurements. The wavelength of the x-ray beam is 0.2952 Å.

The diffraction frame was processed by DIOPTAS with appropriate masking diffraction from diamond and neon [36]. Rietveld refinement for RCrO$_3$ was done with FULLPROF [37], with initial unit-cell parameter obtained from Le Bail profile fitting and atomic positions obtained from the literature. [38–41] The Rietveld refinement for powder x-ray-diffraction patterns of RFeO$_3$ was conducted by RIETAN-FP and VESTA software.

E. Raman measurement

Raman spectra at each pressure were collected in a backscattering configuration with a commercial Renishaw inVia micro-Raman system equipped with a probe laser of 532-nm wavelength. The focused spot size was 2 μm (full width at half maximum, FWHM). Pressures in the chamber were determined by the ruby fluorescence before and after the data collection.

III. RESULTS

The data quality of single-crystal diffraction with a DAC is sensitive to the stress created by the nonhydrostaticity in the pressure medium at higher pressures. In our experiments,

TABLE I. Atomic positions and isotropic displacement parameters (U_{iso}, 10^{-3} Å $[2]$) for orthorhombic perovskite NaOsO$_3$ at 2.5 GPa revealed by refining single-crystal XRD with DAC and the structural data at ambient pressure obtained from single-crystal XRD.

Site	WP[b]	Occp.	x	y	z	U_{iso}
Na	4c	1	$-0.0095(3)$	0.0360(6)	0.25	11.4(6)
			$-0.0090(9)$[a]	0.032(1)[a]		
Os	4b	1	0.5	0	0	8.7(3)
O1	4c	1	0.0831(5)	0.4879(4)	0.25	8.9(7)
			0.078(2)[a]	0.489(1)[a]		
O2	8d	1	0.7059(3)	0.2934(4)	0.042(2)	9.4(5)
			0.711(1)[a]	0.289(1)[a]	0.0396(8)[a]	

[a]Structural data at ambient pressure are after Ref. [42].
[b]Wyckoff positions; space group: *Pbnm* (orthorhombic; No. 62)
Lattice parameters at 2.5 GPa: $a = 5.309(2)$ Å, $b = 5.348(3)$ Å, $c = 7.540(1)$ Å; and $V = 214.1(2)$ Å^3
Lattice parameters at ambient pressure: $a = 5.3382(7)$ Å, $b = 5.3833(7)$ Å, $c = 7.582(1)$ Å; and $V = 217.87(5)$ Å^3.

the stress effect appeared to be negligible since reflection spots and their FWHM in patterns collected were pressure independent to 41.4 GPa. The collected reflections at each pressure ranged from 318 to 469, in which 105–207 unique reflections were used to determine the lattice parameters. The structure refinements were made with the reflections with intensity greater than 3σ (I), where I and σ are the intensity and the standard deviation, respectively. The space group and atomic positions were obtained from the structure refinement. The atomic positions of NaOsO$_3$ at the first pressure point $P = 2.5$ GPa after the DAC was sealed are listed in Table I together with the data at ambient pressure [42]. The small difference of atomic positions between these two sets of data indicates that the intensity correction of diffraction as it goes through diamond anvil is negligible. Lattice parameters from the structure refinement are tabulated in Table II and other relevant parameters associated with the refinement are listed in Table S1 [31].

The single-crystal structure refinements indicate that the *Pbnm* perovskite structure found in NaOsO$_3$ at ambient pressure is stable at pressure to 20 GPa. The values of R_{int} and R_1 for the refinement with the structural model in this pressure range are comparable with other structural studies under high pressure with single-crystal diffraction [43,44], which are indicative of the reliability of the refinement. However, we have some difficulties refining the patterns with the *Pbnm* model in the pressure range of 23.3–29.6 GPa; the refinement leads to a higher value of R_{int} ($>15\%$). The refinements with the *Pbnm* model yield reasonably small R_{int} values at $P > 30$ GPa. To test the possibility that there is a pressure-induced phase in the pressure range of 23.3–29.6 GPa, we have tried to refined the patterns with the polar orthorhombic structure ($Pbn2_1$, No. 33) used by Sereika *et al.* [4] in their structural study with powder diffraction on NaOsO$_3$. The reliability of the refinement was even worse. Given the difficulty to fit the single-crystal diffraction in the pressure range of 23.3–29.6 GPa, we integrated the single-crystal x-ray diffractions into powder-diffraction patterns and refined the

TABLE II. Structure refinement results for perovskite $NaOsO_3$ at high pressures from patterns of single crystal diffraction.

P, GPa	S. G.	a, Å	b, Å	c, Å	V, Å [3]	Unique refl[a]	R_{int}, %	R_1, %
2.5(1)	*Pbnm*	5.309(2)	5.348(3)	7.540(1)	214.1(2)	151	0.48	3.73
4.2(1)	*Pbnm*	5.283(1)	5.333(2)	7.513(1)	211.7(1)	202	0.47	4.67
6.7(1)	*Pbnm*	5.245(1)	5.322(2)	7.4750(8)	208.64(9)	207	0.43	3.65
8.1(1)	*Pbnm*	5.226(2)	5.307(3)	7.454(1)	206.8(1)	195	0.38	3.82
11.1(1)	*Pbnm*	5.187(1)	5.290(2)	7.4143(7)	203.44(7)	176	0.7	5.06
14.6(1)	*Pbnm*	5.156(1)	5.266(2)	7.3789(9)	200.34(9)	169	0.72	3.12
15.6(1)	*Pbnm*	5.138(2)	5.263(3)	7.363(1)	199.1(1)	177	0.85	4.88
17.8(5)	*Pbnm*	5.126(4)	5.241(6)	7.343(2)	197.3(3)	119	4.64	6.32
20.0(1)	*Pbnm*	5.086(3)	5.236(5)	7.311(2)	194.7(2)	126	3.42	5.70
31.2(1)	*Pbnm*	4.949(4)	5.228(3)	7.220(2)	186.8(2)	137	2.21	4.75
33.3(1)	*Pbnm*	4.918(5)	5.226(3)	7.196(2)	185.0(2)	131	1.93	5.50
36.3(2)	*Pbnm*	4.913(5)	5.20(1)	7.171(4)	183.2(5)	105	1.78	6.31
39.0(1)	*Pbnm*	4.892(6)	5.184(1)	7.151(4)	181.4(2)	112	3.11	7.27
41.4(1)	*Pbnm*	4.883(7)	5.16(1)	7.141(5)	179.8(5)	140	3.08	6.44

[a]Unique refl: number of unique reflections used in refinement.

integrated powder patterns with the Le Bail analysis method. The refinements with either the *Pbnm* structural model or the $Pbn2_1$ structural model gave nearly the same R value; see the detailed refinement results in Table S2. Moreover, the lattice parameters obtained in this analysis connected smoothly to those at lower pressures ($P \leqslant 20$ GPa) and higher pressures ($P > 30$ GPa), as shown in Fig. 2(a). In addition, we have

FIG. 2. Pressure dependences of (a) lattice parameters, (b) cell volume and the fitting result to the BM equation, and (c) reduced S factor $S_r = [S(P) - S(0)]/S(0)$ for $NaOsO_3$. Simulation results in (a) are after Ref. [72].

tried to refine the single-crystal diffraction patterns above 30 GPa with the polar orthorhombic structural model ($Pbn2_1$).

Furthermore, we employed the methodology described in the literature [45] to determine the appropriate space group for $NaOsO_3$ at different pressure points. The structures of $NaOsO_3$ at each pressure point were initially refined with the $Pbn2_1$ structural model since the symmetry of $Pbn2_1$ is lower than *Pbnm*. The program was utilized to search for an appropriate higher symmetry group for the structure at each pressure points. Notably, the *Pbnm* space group was unambiguously suggested by PLATON for the low-pressure structure of $NaOsO_3$ ($P \leqslant 15.6$ GPa). However, this method turned out to be unreliable for the diffraction patterns at higher pressures since it did not give a consistent suggestion for the symmetry. The comparison of refinement results between these two orthorhombic structure solutions is tabulated in Table S1 [31].

In a separate experiment (EXP2), we checked another piece of $NaOsO_3$ crystal at several pressure points in the range of 20 to 30 GPa. The single-crystal diffraction patterns can be refined well with the *Pbnm* structural model; see the results in Table S3 [31]. Since the experiment was done on a different crystal with a different DAC at separated beamline time, there were small offsets between two sets of data.

As shown in Fig. 2(a), the enlarged orthorhombic distortion under high pressure as indicated by the lattice parameter splitting from $P \geqslant 2.5$ GPa contradicts a slightly reduction of the lattice-parameter splitting from ambient pressure to 2.5 GPa. It is difficult for us to distinguish whether the lattice parameters' anomaly at 2.5 GPa is a real pressure effect or an offset between the data collected at ambient pressure reported in the literature and the data collected with a DAC in this work. Nevertheless, the cell volume decreases smoothly under pressure from the cell volume V_{am} at ambient pressure from the literature. The $V(P)$ in the entire pressure range to 41 GPa has been fit to the Birch-Murnaghan (BM) equation in Fig. 2(b); the V_0 from the fitting matches V_{am} well. The pressure dependence of lattice parameters reveals two important features in $NaOsO_3$: (1) the orthorhombic distortion as measured by the S factor $S = (b - a)/(b + a)$ displayed in Fig. 2(c) increases more drastically, and (2) the bulk modulus $B_0 = 152$ GPa is unusually low in comparison with
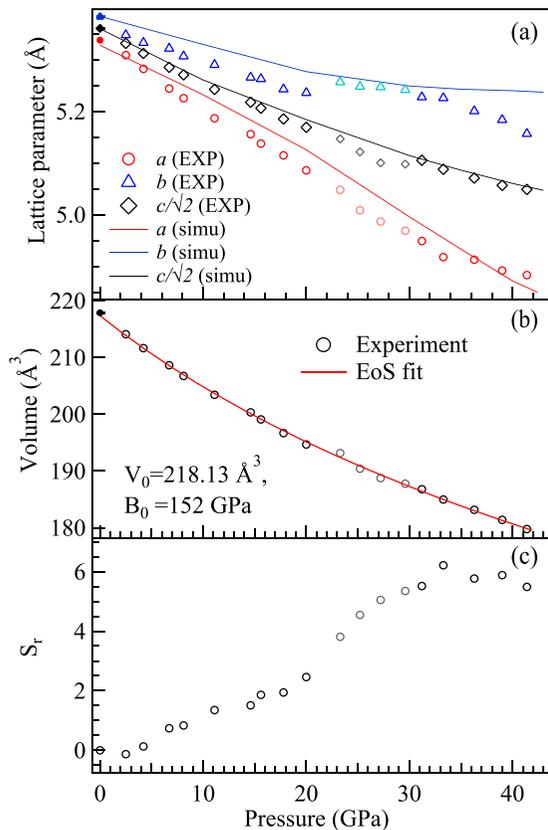
most orthorhombic perovskites in the literature. These observations are consistent with the results reported by Sereika *et al.* [4].

Figure 1 displays the structural distortions allowed by the symmetry in the *Pbnm* orthorhombic perovskite ABO_3 consisting of three major components, i.e., the octahedral-site rotations around the 110 axis (θ) (major) and 001 axis (ϕ) (minor) of the primary cell and the *A*-site cation shifting away from the position in the cubic perovskite, and minor octahedral-site distortions, i.e., the bond-length splitting and the O_{21}-*B*-O_{22} bond angle α deviating from 90° in a BO_6 octahedron. The octahedral-site rotation around the 110 axis of the primary cell or the *b* axis of the orthorhombic cell makes the BO_2 plane buckle along the *a* axis, which leads to the lattice parameter $a < c/\sqrt{2} < b$ for rigid octahedra. However, lattice parameters $a > b$ are found in the orthorhombic perovskites where the O_{21}-*B*-O_{22} (α opening to the *a* axis) is slightly less than 90°. The simulated perovskite structure with the structural prediction software SPUDS is a good reference for estimating whether the local structural distortion occurs from the lattice parameters. First, lattice parameters $b > a$ hold in all *Pbnm* perovskites predicted by using SPUDS since the assumption of rigid octahedron is used. It has been demonstrated in the $A^{3+}B^{3+}O_3$ perovskites that $(b$-$a)_{\text{sim}} < (b$-$a)_{\text{obs}}$ in the perovskites where the octahedral-site distortions are very small or negligible, whereas $(b$-$a)_{\text{sim}} > (b$-$a)_{\text{obs}}$ holds where the distortions occur [46]. This criterion is useful since an accurate determination of the O_{21}-*B*-O_{22} bond angle is difficult even with neutron diffraction. The connection between a slightly enhanced $(b$-$a)$ and the α angle on cooling through the metal-insulator transition temperature T_{MIT} in NaOsO$_3$ cannot be verified by neutron diffraction since the change of α is within error bars [47]. The observation of $(b$-$a)_{\text{sim}} < (b$-$a)_{\text{obs}}$ in NaOsO$_3$ indicates the α angle is close to 90°.

Results from refining single-crystal diffraction provide the detailed information how these components of the orthorhombic distortion change under high pressure. As shown in Fig. 3(a), the α angle increases modestly under pressure to 20 GPa closing to 90°, followed by a pronounced jump to 90.5° at $P > 30$ GPa. At ambient pressure, NaOsO$_3$ is in the group of perovskites with the smallest bond-length splitting. Within the error bars, pressure does not change the bond-length splitting up to $P \sim 15$ GPa as shown in Fig. 3(b). An obvious bond-length splitting occurs above 15 GPa and the splitting is further enhanced at higher pressures. The octahedral-site rotation angles θ and ϕ are not measurable directly from the structural model in refinement results, but can be derived through the geometric relations of method I: lattice parameters only; method II: atomic positions and the lattice parameters; and method III: the bond angles as summarized in Table S4. These methods are valid only if these rotation angles are small [48]. The derived rotation angles are displayed in Fig. 3(c). The θ and ϕ from methods II and III are highly consistent; both the θ and the ϕ angles increase with increasing pressure. Due to the octahedral-site distortions, these angles derived from method I are smaller than those from methods II and III at low pressures. However, all three methods give a $\theta \sim 18$° and $\phi \sim 14$° at the highest pressure in our experiment. In NaO$_x$ polyhedra of the orthorhombic perovskite NaOsO$_3$, Na moves from the center along the (100)
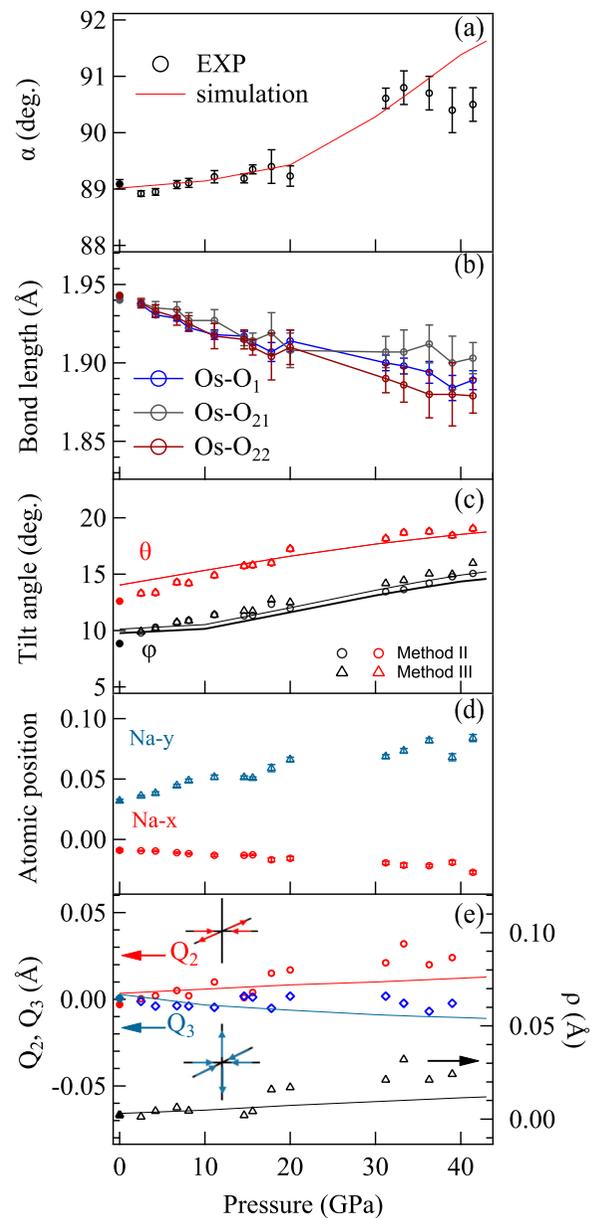
FIG. 3. Pressure dependences of local distortions in NaOsO$_3$ (a) the O_{21}-Os-O_{22}; (b) the Os-O bond length; (c) the tilting angles as defined in Fig. 1; (d) the Na position in the structure; (e) the orthorhombic modes Q_2 and Q_3. Lines in (b) are guides to eyes; the simulation results of θ and ϕ angles in (c) are obtained through methods II and III; see formula in Table S4. Simulation results in (a), (c), and (e) are after Ref. [72]. Solid symbols represent structural data at ambient pressure after Ref. [42].

axis of the primary cell; the displacement increases monotonically under pressure as shown in Fig. 3(d).

To support the argument of a pressure-induced phase transition in NaOsO$_3$, Sereika *et al.* [4] have demonstrated the discontinuous changes of phonon modes by Raman spectroscopy on crossing 18 GPa. The Grűneisen constants of all Raman-active modes change at $P \sim 18$ GPa. We have performed the Raman measurement on a well-polished NaOsO$_3$ crystal chip. The number of major Raman-active modes near ambient pressure was the same as that reported by Sereika
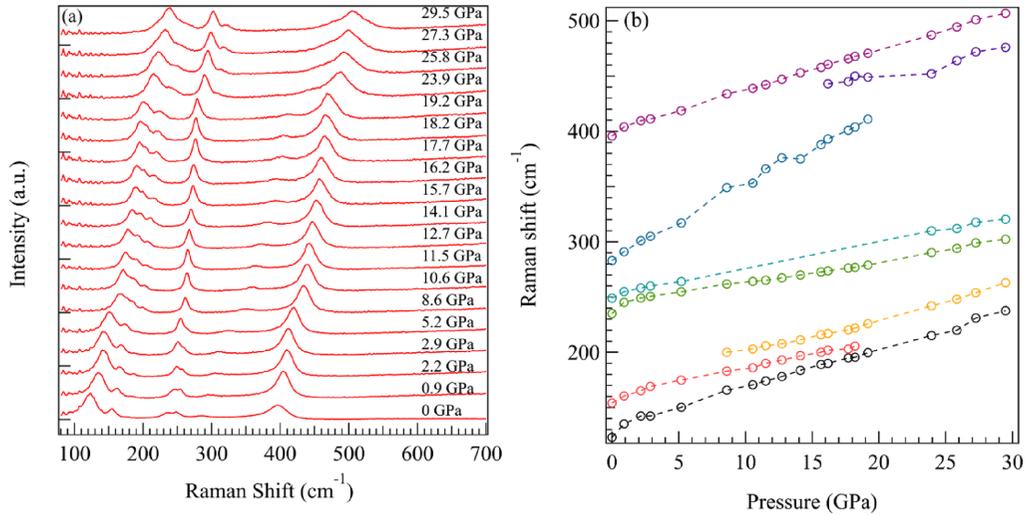
FIG. 4. (a) Raman spectra of single-crystal $NaOsO_3$ at different pressures. (b) Pressure dependence of Raman-active modes.

et al. [4] As displayed in Fig. 4, only one mode at $290\,cm^{-1}$ disappears at $P \sim 19\,GPa$; all other modes change smoothly in the entire pressure range to 30 GPa. In the perovskite $PbRuO_3$, the pressure-induced phase transition from the *Pbnm* to the $Pbn2_1$ phase corresponds to a pronounced change of Raman spectroscopy [14]. It is clearly not the case in $NaOsO_3$.

Figures 5 and 6 display the refinement results from powder diffraction on perovskites $RCrO_3$ and $RFeO_3$. All data associated with the refinement are provided in Tables S5–S10 [31]. At ambient pressure, the orthorhombic distortion increases smoothly as the rare-earth ionic size decreases from La to Lu in these two families of perovskites. We have selected three members in each of two families for the high-pressure structural study; the RMO_3 with $R = Lu$ and Tm have a larger orthorhombic distortion, whereas the distortion is much smaller in $NdMO_3$. There is a clear trend from the results of the high-pressure structural study: the distortion becomes even smaller under pressure in those with small orthorhombic distortion, whereas the distortion increases under pressure in those with large orthorhombic distortion. In addition, pressure induces a phase transition from the *Pbnm* phase to the $R3\text{-}c$ phase following the lattice-parameter crossover from $b > a$ to $b < a$ in the *Pbnm* phase, which has been found in other perovskites [49–54]. In $RFeO_3$, high pressure induces a spin-state transition [55–57], which interferes with the pressure dependence of the crystal structure found in most perovskite oxides without spin-state transition. The phase transition from the low-pressure phase to the high-pressure phase found in $NdFeO_3$ and $LuFeO_3$ matches that reported in the literature very well.

IV. DISCUSSION

A. dt/dP in the orthorhombic perovskites

Determination of complete crystal structure of $NaOsO_3$ under high pressure, which is the only case for the $5d$ perovskite oxide so far, adds a fresh input to address the long-standing question: is there a universal rule of how the crystal structure responds to hydrostatic pressure? In a brief survey of the

existing studies of perovskite oxides under high pressure, the sign of dt/dP has little to do with the charge distribution in the ABO_3 formula. Figure 7 displays the reduced S factor for a variety of perovskites with different charge configurations. There appears a general trend from this plot. In the group of perovskites with a small $|dt/dP|$, both positive and negative dt/dP can be found.

For the $R^{3+}M^{3+}O_3$ perovskites ($R=$ rare earth), the value of $|dt/dP|$ is small. The sign change of $|dt/dP|$ in this group can be explained by the variations of bond lengths obtained through a complete structural determination under pressure. In a systematic structural study, Zhou and Goodenough [58] pointed out that the bond-length splitting of MO_6 octahedron does not show a monotonic dependence of the t factor but a maximum in the middle of the t factor span in each family of the transition-metal oxides, RMO_3. Zhou [30] has further put forward a hypothesis that the essential pressure effect on the perovskite structure is to reduce the bond-length splitting in MO_6 octahedra. Pressure increases the orthorhombic distortion for the RMO_3 with smaller rare earths, whereas it reduces the distortion for the RMO_3 with larger rare earths. Although the structural data for $A^{2+}B^{4+}O_3$ in the literature are incomplete for a comparative study, a $dt/dP < 0$ found in $CaTiO_3$ ($t = 0.9464$) and $dt/dP > 0$ in $CaGeO_3$ ($t = 0.9788$) are consistent with the general trend of pressure effect in the $R^{3+}M^{3+}O_3$ perovskites.

For the ABO_3 perovskite with B elements in $4d$ and $5d$ rows, however, a $dt/dP < 0$ has been obtained universally. The transition from a small coefficient $\pm|dt/dP|$ in the $3d$ perovskites to a negative dt/dP with a larger magnitude in $4d$ and $5d$ perovskites could be possibly rationalized by the consideration of bond-valence sum. The structural data and the BVS derived for typical perovskites with the B-site elements covering $3d$, $4d$, and $5d$ rows are listed in Table III. In comparing with their formal valance, B-O in the $3d$ perovskites are overbonding, whereas it is underbonding in $4d$ and $5d$ perovskites. Moreover, it appears that BO_6 octahedra are much less compressible in those perovskites with the underbonding B-O bonds than that with the overbonding B-O bonds; for example, $\beta = 1.722 \times 10^{-3}\,GPa^{-1}$ in $GdFeO_3$,
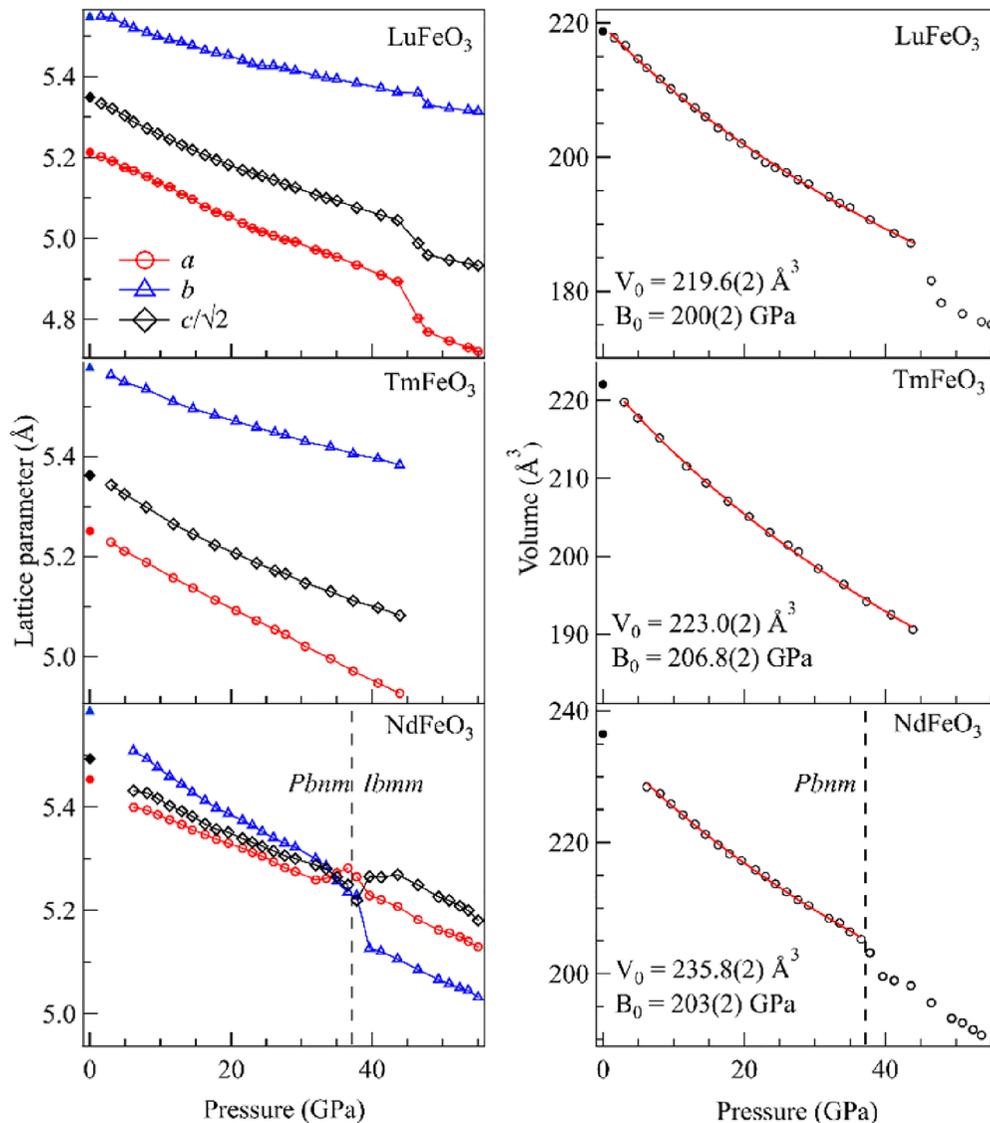
FIG. 5. Pressure dependences of lattice parameters of $RFeO_3$.

$1.59 \times 10^{-3}\,GPa^{-1}$ in $CaSnO_3$, and $9.22 \times 10^{-4}\,GPa^{-1}$ in $NaOsO_3$. The smaller compressibility of BO_6 explains a $dt/dP < 0$ in the $4d$ and $5d$ perovskites.

B. The local structural change under high pressure

A BO_6 octahedron in the orthorhombic perovskite can undergo two kinds of distortions, i.e., the bond-length splitting and the α angle deviating from $90°$. Whereas the pressure effect has been postulated to reduce the bond-length splitting at the expense of octahedral-site rotations and the A-site cation dislocation [30], how the α angle changes under pressure has been overlooked in the structural studies under high pressure in the literature. The bond-length splitting in $NaOsO_3$ does not shows any discernible change with the experimental resolution at pressures to 15 GPa. An extremely small compressibility in OsO_6 octahedron is accommodated by the octahedral-site rotations that lead to a continuous increase of the S factor. Moreover, a gradual increase of the α angle toward $90°$ under pressure also contributes to the increase of

S in this pressure range through the relationship

$$b = b_u[\sqrt{2}\cos(45 + \alpha/2)],$$
$$a = a_u[\sqrt{2}\sin(45 + \alpha/2)], \qquad (2)$$

where a_u and b_u are the lattice parameters for the cell with rigid octahedra [59]. The rule of holding or reducing the bond-length splitting in OsO_6 octahedron under pressure at $P < 15$ GPa collapses at $P > 15$ GPa. Given a smooth increase of the rotation angles θ and ϕ, an obvious slope change at $P \sim 15$ GPa in S vs P in Fig. 2(c) can only be contributed by abrupt changes of the bond-length splitting and the angle α in OsO_6 octahedron. Severe octahedral-site rotation around a fixed axis is not compatible with rigid OsO_6 octahedra [60]. Pressure appears to induce a major structural change within the Pbnm space group. The low-pressure phase has $\alpha < 90°$, whereas the high-pressure phase has $\alpha > 90°$. The two-phase coexistence in the pressure range 20–30 GPa causes difficulties in the structural refinement of the single-crystal patterns. Powder diffraction does not convey enough information to
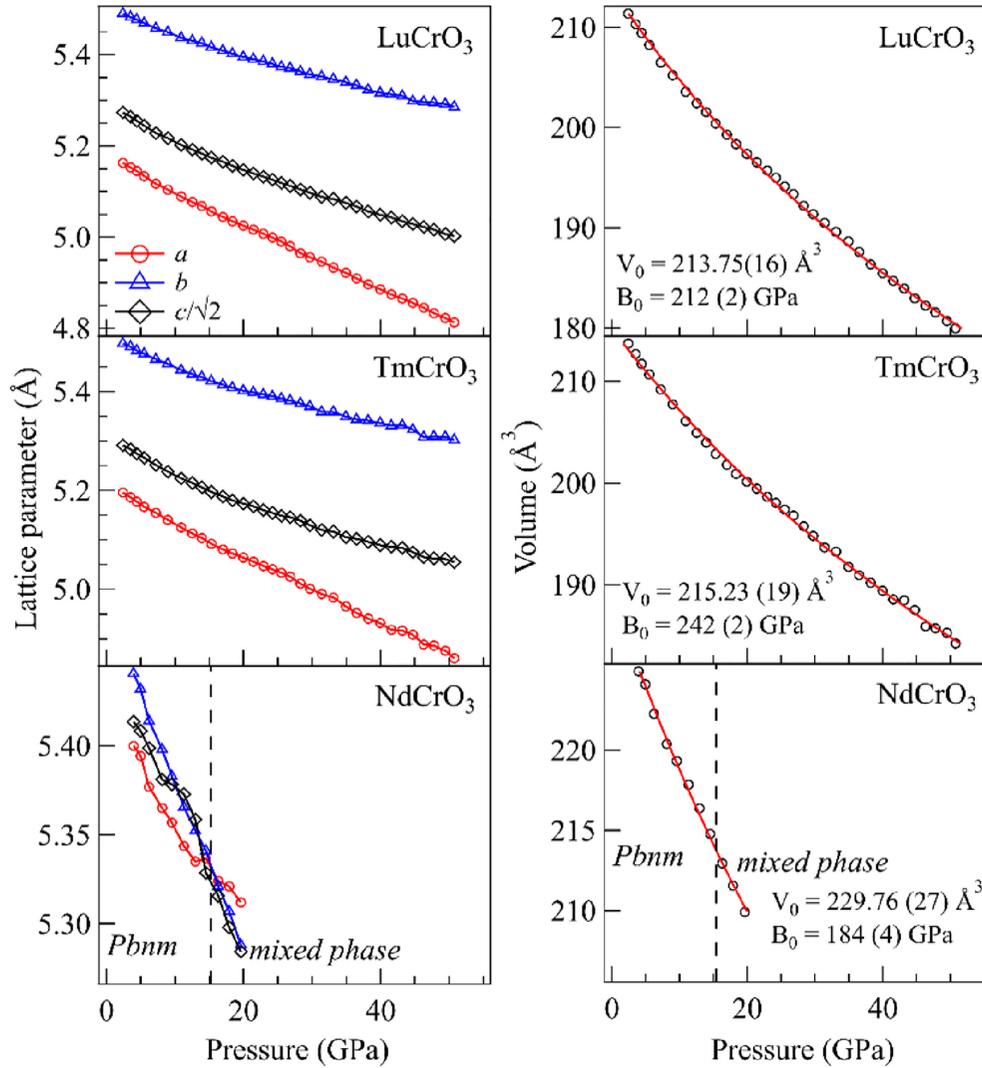
FIG. 6. Pressure dependences of lattice parameters and the fitting results to the BM equation of $R\text{CrO}_3$.
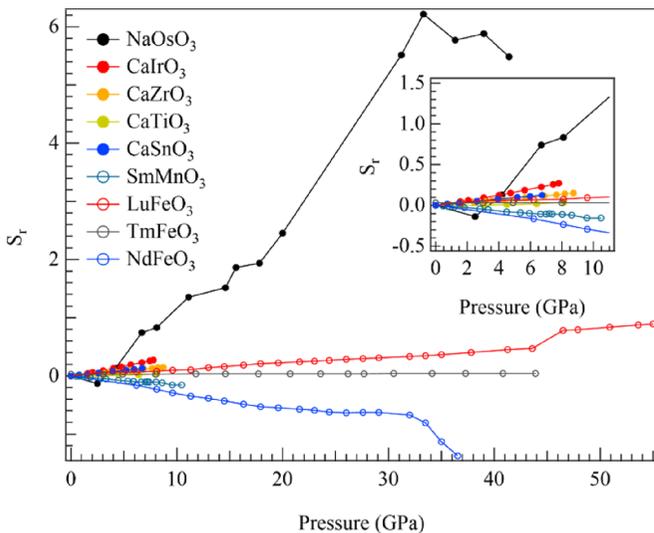
FIG. 7. Pressure dependence of reduced S factors for *Pbnm* perovskites.

resolve precisely the local distortion. The complicated diffraction patterns due to the two-phase coexistence and highly distorted local structures could mislead Sereika *et al.* [4] to refine the data with a lower-symmetry polar structural model, $Pbn2_1$.

The local distortion in NaOsO_3 is similar to the intrinsic structural distortion of the *Pbnm* perovskite identified in the $3d$ perovskites [58], which is exemplified by the $R\text{FeO}_3$ family since Fe^{3+} is not Jahn-Teller (JT) active. The Fe-O bond length along x,y,z of the primary cell direction can be organized in the two orthorhombic displacement modes:

$$Q_2 = l_x - l_y \quad \text{and} \quad Q_3 = (2l_z - l_x - l_y)/\sqrt{3}. \quad (3)$$

At ambient pressure, the local distortion of NaOsO_3 is close to that of LaFeO_3 since $\text{Os}^{5+}(t_{2g}^3 e_g^0)$ is not JT active. Pressure enlarges the local distortion in NaOsO_3 as displayed in Fig. 3(e). In the (Q_2, Q_3) space, the local distortion of $R\text{FeO}_3$ increases from origin for $R = \text{La}$ long $150°$ ($210°$) to the maximum at $R = \text{Gd}$ and then reduces on a different wing as the rare-earth size further reduces from Gd. The

TABLE III. Comparison of bond-valence sums (BVSs) of orthorhombic perovskite oxides at ambient pressure and room temperature.

		NaOsO$_3$ (this work)	CaTiO$_3$ (Ref. [74])	CaZrO$_3$ (Ref. [75])	CaGeO$_3$ (Ref. [76])	CaSnO$_3$ (Ref. [77])	GdFeO$_3$ (Ref. [39,64])
Space group		*Pbnm*	*Pbnm*	*Pbnm*	*Pbnm*	*Pbnm*	*Pbnm*
Lattice parameter (Å)	a	5.3382(7)	5.3796(1)	5.59111(7)	5.2607(6)	5.532(2)	5.349
	b	5.3833(7)	5.4423(3)	5.76128(8)	5.269(1)	5.681(2)	5.611
	c	7.582(1)	7.6401(5)	8.0169(1)	7.445(2)	7.906(2)	7.669
Bond length of *B*-O (Å)		1.942(3) × 2	1.9503(3) × 2	2.09893(3) × 2	1.889(9) × 2	2.063(2) × 2	1.99968 × 2
		1.940(6) × 2	1.9551(8) × 2	2.0913(6) × 2	1.898(3) × 2	2.061(4) × 2	2.02736 × 2
		1.943(6) × 2	1.9587(8) × 2	2.0984(6) × 2	1.889(3) × 2	2.061(4) × 2	2.00979 × 2
BVS at *B* site[a]		4.92	4.11	3.90	4.07	3.93	3.03
Compressibility of *B*-O bond (GPa^{-1})		-9.22×10^{-4}	-1.51×10^{-3}			-1.59×10^{-3}	-1.72×10^{-3}

[a]BVS = $\sum_{i=1}^{N} v_i$, where $v_i = e^{(R_0 - l_i)/B}$, N is the coordination number, l is the bond length, $B = 0.37$, $R_0(\text{Os}^{5+}) = 1.868$ [78], $R_0(\text{Zr}^{4+}) = 1.937$, $R_0(\text{Ti}^{4+}) = 1.815$, $R_0(\text{Ge}^{4+}) = 1.748$, $R_0(\text{Sn}^{4+}) = 1.905$, and $R_0(\text{Fe}^{3+}) = 1.759$ [79]. The compressibility of *B*-O bond for CaTiO$_3$ and CaSnO$_3$ are calculated from the bond length reported in Refs. [80,81].

pressure effect on the local distortion in NaOsO$_3$ is close to the change from LaFeO$_3$ to GdFeO$_3$. The magnitude of the local distortion $r = (Q_2^2 + Q_3^2)^{1/2}$ at 40 GPa is comparable to that in GdFeO$_3$.

C. The bulk modulus

The cell volume of NaOsO$_3$ versus pressure in Fig. 2(c) fits well the Birch-Murnaghan equation with a fixed $B\prime = 4$. The bulk modulus $B = 152$ GPa obtained which is close to that from powder diffraction [4] is smaller than most perovskite oxides. NaOsO$_3$ stands out in the plot of B_0 vs $1/V_0$ along with other perovskite oxides in Fig. 8. Anderson *et al.* have summarized the data of a vast number of compounds in a plot of B_0 vs $1/V_0$ and found a $B_0 V_0 = $ constant [61,62]. This rule works well in the system with a simpler structure but the volume varies in a broad range. In perovskite oxides, the overall change of the cell volume is small. Other factors,
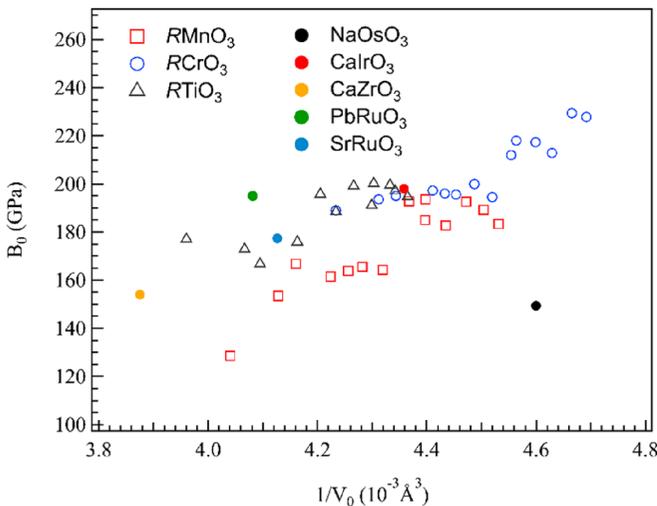
FIG. 8. Bulk modulus vs inverse cell volume for orthorhombic perovskite oxides including 3*d* RMO$_3$ (R = rare earth; M = Ti, Cr, Mn) [30]; 4*d* CaZrO$_3$ [27], PbRuO$_4$ [14], and SrRuO$_4$ [73]; 5*d* NaOsO$_3$ (this work) and CaIrO$_3$ [29].

such as the onset of local distortion described by the α angle in an octahedron, can induce large anomalies in the plot of B_0 vs $1/V_0$. There is a major anomaly in the plot for each family of 3*d* perovskite oxides at the point where α starts to deviate from 90°. Nevertheless, a perovskite with a smaller cell volume generally has a larger B_0. It is highly unusual that NaOsO$_3$ with the cell volume at the low end among perovskite oxides shows a small B_0.

In the orthorhombic perovskite ABO$_3$, reducing the cell volume can be accomplished by either shrinking the BO$_6$ octahedral volume or enlarging the octahedral-site rotation. The contribution to the cell compressibility from these two components can be expressed as [63]

$$\beta_v = \beta_{(B\text{-}O)} + \beta_\Phi = -3(B\text{-}O)^{-1}d(B\text{-}O)/dP$$
$$- 2\cos^{-1}\Phi d(\cos\Phi)/dP . \quad (4)$$

The tilting angle Φ is the combination of θ and φ shown in Fig. 1 and is calculated through $\cos\Phi = \cos\theta\cos\varphi$. Taking GdFeO$_3$ for example, $\beta_{(\text{Fe-O})} = 5.17 \times 10^{-3}$ GPa^{-1} dominates in β_v. In this 3*d* perovskite oxide, the tilting angle Φ decreases slightly under pressure, resulting in a negative $\beta_\Phi = -2.7 \times 10^{-4}$ GPa^{-1}. The bulk modulus calculated from the local structure change under pressure $\beta_v^{-1} = 204$ GPa is larger than $B_0 = 182$ from fitting the cell volume versus pressure [64]. In sharp contrast, a smaller $\beta_{(\text{Os-O})} = 2.7 \times 10^{-3}$ GPa^{-1} and a giant $\beta_\Phi = 2.8 \times 10^{-3}$ GPa^{-1} are obtained for NaOsO$_3$. A lower $\beta_v^{-1} = 179$ GPa is consistent with $B_0 = 149$ GPa from fitting the plot of V vs P. The data of local structure normally come with larger error bars. β_v in Eq. (4) is the compressibility of matter at $P = 0$ GPa.

There is a clear trend of progressively decreasing $\beta_{(B\text{-}O)}$ in ABO$_3$ perovskites from the 3*d* to the 4*d* and the 5*d* row of elements. The $\beta_{(B\text{-}O)}$ in NaOsO$_3$ is the smallest based on the available data. The crystal symmetry in the orthorhombic perovskite structure allows for the tilting of octahedra, which in turn enables the lattice to be compressed. Although $\beta_{(B\text{-}O)}$ in KOsO$_3$ is larger than that in NaOsO$_3$ [65], the tilting degree of freedom is eliminated in the cubic structure, resulting in a smaller β_v and a higher bulk modulus compared to other perovskite oxides.

D. The comparison with first-principles calculation

Although some phenomenological rules such the Anderson rule [61,62] and the Bloch rule [66] have been rationalized by the microscopic theories [62,67,68], analytical approaches fall far behind the demand for the high-precision simulations that could replace the costlier experimental efforts in the material research in the future. The combination of strong computation power and the first-principles calculation has enabled high-precision simulations of vast amounts of material systems. In the case of perovskite oxides, significant progress has been made in predicting crystal structures that match the experimental results to the third or fourth decimal place [69,70]. For simulating pressure effects on the perovskite structure, Xiang *et al.* [71] predicted a $dt/dP < 0$ for the most $A^{2+}B^{4+}O_3$ perovskites with a $t \leqslant 1$. For $A^{3+}B^{3+}O_3$ perovskites, they calculated a $dt/dP > 0$ for the perovskites with a t factor in the high end of this group, and a dt/dP approaching zero for those with the t factor in the low end of the group. The experimental finding of a $dt/dP > 0$ in $CaGeO_3$ contradicts this prediction. While the trend of decreasing magnitude of dt/dP as the t factor decreases is consistent with the experimental results for some $A^{3+}B^{3+}O_3$ perovskites, further improvements are necessary to order to account for a $dt/dP < 0$ in the $A^{3+}B^{3+}O_3$ perovskites with a low t factor.

In the calculation [71], an overwhelming $dt/dP < 0$ has been predicted for $A^{1+}B^{5+}O_3$ perovskites, such as $LiTaO_3$ and $LiNbO_3$, which is consistent with the results of $NaOsO_3$ reported in this work. The simulated results for $NaOsO_3$ under pressure have been reported in the literature [72]. The simulated changes in lattice parameters and the local structure under pressure match the experimental observations remarkably well, as evidenced by superimposition of predicted values with experimental data in the corresponding figures: Fig. 2(a) and Figs. 3(a), 3(c), and 3(e).

V. CONCLUSION

At ambient pressure, $NaOsO_3$ exhibits a relatively small orthorhombic distortion compared to a large group of orthorhombic perovskite oxides. However, hydrostatic pressure enhances significantly the orthorhombic distortion by enlarging the OsO_6 octahedral-site tilting. The local structural distortions, as measured by the O_{21}-Os-O_{22} bond angle (α) and the Os-O bond-length splitting, show modest changes under pressure up to 15 GPa. Pressure induces a phase transition from the phase with $\alpha < 90°$ to the phase with $\alpha > 90°$ at $P \geqslant 30$ GPa, with two-phase coexistence at $20 < P <$ 30 GPa. However, the *Pbnm* phase remains the most suitable structural model from the refinements in the entire pressure range. In the pressure range where two-phase coexistence is found, there are some difficulties in refining single-crystal diffraction patterns by a single-phase structural model.

In the orthorhombic perovskite ABO_3, the volume reduction can be made through (1) reducing the volume of BO_6 octahedra and (2) increasing the octahedral-site rotations. Our structural study of $NaOsO_3$ indicates that although the OsO_6 octahedra are the least compressible among perovskite oxides, the significant octahedral-site rotations under pressure contribute nearly 50% of the cell compressibility, which accounts for a much lower bulk modulus found in $NaOsO_3$.

In contrast to the 5d perovskite $NaOsO_3$, the orthorhombic structural distortion changes modestly under pressure in the 3d transition-metal perovskite oxides with the $A^{3+}B^{3+}O_3$ charge configuration. It is important to note that in this group of perovskites, the orthorhombic distortion reduces under pressure in the perovskites with less orthorhombic distortion at ambient pressure, whereas it increases under pressure in the perovskites with larger orthorhombic distortion at ambient pressure.

[1] Y. Shi, Y. Guo, X. Wang, A. J. Princep, D. Khalyavin, P. Manuel, Y. Michiue, A. Sato, K. Tsuda, S. Yu, M. Arai, Y. Shirako, M. Akaogi, N. Wang, K. Yamaura, and A. T. Boothroyd, A ferroelectric-like structural transition in a metal, Nat. Mater. **12**, 1024 (2013).

[2] J. C. Slater, Magnetic effects and the Hartree-Fock equation, Phys. Rev. **82**, 538 (1951).

[3] J. G. Vale, S. Calder, C. Donnerer, D. Pincini, Y. G. Shi, Y. Tsujimoto, K. Yamaura, M. Moretti Sala, J. van den Brink, A. D. Christianson, and D. F. McMorrow, Evolution of the magnetic excitations in $NaOsO_3$ through its metal-insulator transition, Phys. Rev. Lett. **120**, 227203 (2018).

[4] R. Sereika, P. Liu, B. Kim, S. Kim, J. Zhang, B. Chen, K. Yamaura, C. Park, C. Franchini, Y. Ding, and H. k. Mao, Aberrant electronic and structural alterations in pressure tuned perovskite $NaOsO_3$, npj Quantum Mater. **5**, 66 (2020).

[5] X. Obradors, L. M. Paulius, M. B. Maple, J. B. Torrance, A. I. Nazzal, J. Fontcuberta, and X. Granados, Pressure

dependence of the metal-insulator transition in the charge-transfer oxides RNiO$_3$ (R = Pr, Nd, Nd$_{0.7}$La$_{0.3}$), Phys. Rev. B **47**, 12353 (1993).

[6] P. C. Canfield, J. D. Thompson, S. W. Cheong, and L. W. Rupp, Extraordinary pressure dependence of the metal-to-insulator transition in the charge-transfer compounds NdNiO$_3$ and PrNiO$_3$, Phys. Rev. B **47**, 12357 (1993).

[7] J. S. Zhou, J. B. Goodenough, B. Dabrowski, P. W. Klamut, and Z. Bukowski, Probing the metal-insulator transition in Ni(III)-oxide perovskites, Phys. Rev. B **61**, 4401 (2000).

[8] J. S. Zhou, J. B. Goodenough, and B. Dabrowski, Pressure-induced non-fermi-liquid behavior of PrNiO$_3$, Phys. Rev. Lett. **94**, 226602 (2005).

[9] G. A. Samara, T. Sakudo, and K. Yoshimitsu, Important generalization concerning the role of competing forces in displacive phase transitions, Phys. Rev. Lett. **35**, 1767 (1975).

[10] A. Al-Zein, P. Bouvier, A. Kania, C. Levelut, B. Hehlen, V. Nassif, T. C. Hansen, P. Fertey, J. Haines, and J. Rouquette, High pressure single crystal x-ray and neutron powder diffraction study of the ferroelectric–paraelectric phase transition in PbTiO$_3$, J. Phys. D: Appl. Phys. **48**, 504008 (2015).

[11] S. K. Mishra, M. K. Gupta, R. Mittal, S. L. Chaplot, and T. Hansen, Suppression of antiferroelectric state in NaNbO$_3$ at high pressure from in situ neutron diffraction, Appl. Phys. Lett. **101**, 242907 (2012).

[12] E. I. Paredes Aulestia, Y. W. Cheung, Y.-W. Fang, J. He, K. Yamaura, K. T. Lai, S. K. Goh, and H. Chen, Pressure-induced enhancement of non-polar to polar transition temperature in metallic LiOsO$_3$, Appl. Phys. Lett. **113**, 012902 (2018).

[13] J. J. Gao, S. Y. Fu, K. Yamaura, J. F. Lin, and J. S. Zhou, Room-temperature polar metal stabilized under high pressure, Phys. Rev. B **101**, 220101(R) (2020).

[14] J. G. Cheng, K. E. Kweon, J. S. Zhou, J. A. Alonso, P. P. Kong, Y. Liu, C. Jin, J. Wu, J.-F. Lin, S. A. Larregola, W. Yang, G. Shen, A. H. MacDonald, A. Manthiram, G. S. Hwang, and J. B. Goodenough, Anomalous perovskite PbRuO$_3$ stabilized under high pressure, Proc. Natl. Acad. Sci. **110**, 20003 (2013).

[15] J. B. Torrance, P. Lacorre, A. I. Nazzal, E. J. Ansaldo, and Ch. Niedermayer, Systematic study of insulator-metal transitions in perovskites RNiO$_3$ (R = Pr, Nd, Sm, Eu) due to closing of charge-transfer gap, Phys. Rev. B **45**, 8209 (1992).

[16] J. L. García-Muñoz, J. Rodríguez-Carvajal, P. Lacorre, and J. B. Torrance, Neutron-diffraction study of RNiO$_3$ (R = La, Pr, Nd, Sm): Electronically induced structural changes across the metal-insulator transition, Phys. Rev. B **46**, 4414 (1992).

[17] S. Miyasaka, Y. Okimoto, M. Iwama, and Y. Tokura, Spin-orbital phase diagram of perovskite-type RVO$_3$ (R = rare-earth ion or Y), Phys. Rev. B **68**, 100406(R) (2003).

[18] J. S. Zhou, J. A. Alonso, V. Pomjakushin, J. B. Goodenough, Y. Ren, J. Q. Yan, and J. G. Cheng, Intrinsic structural distortion and superexchange interaction in the orthorhombic rare-earth perovskites RCrO$_3$, Phys. Rev. B **81**, 214115 (2010).

[19] J. Q. Yan, J. S. Zhou, and J. B. Goodenough, Bond-length fluctuations and the spin-state transition in LCoO$_3$ (L = La Pr, and Nd), Phys. Rev. B **69**, 134409 (2004).

[20] J. S. Zhou and J. B. Goodenough, Pressure-induced transition from localized electron toward band antiferromagnetism in LaMnO$_3$, Phys. Rev. Lett. **89**, 087201 (2002).

[21] J. S. Zhou, G. L. Liu, and J. B. Goodenough, Pressure-induced transitions in single-crystal La$_{0.84}$Sr$_{0.16}$MnO$_3$, Phys. Rev. B **63**, 172416 (2001).

[22] J. S. Zhou, J. Q. Yan, and J. B. Goodenough, Bulk modulus anomaly in RCoO$_3$ (R = La, Pr, and Nd), Phys. Rev. B **71**, 220103(R) (2005).

[23] T. Vogt, J. A. Hriljac, N. C. Hyatt, and P. Woodward, Pressure-induced intermediate-to-low spin state transition in LaCoO$_3$, Phys. Rev. B **67**, 140401(R) (2003).

[24] J. S. Zhou, J. B. Goodenough, J. Q. Yan, J. G. Cheng, K. Matsubayashi, Y. Uwatoko, and Y. Ren, Orbital hybridization in RVO$_3$ perovskites: A high-pressure study, Phys. Rev. B **80**, 224422 (2009).

[25] J. S. Zhou, J. A. Alonso, J. Sanchez-Benitez, M. T. Fernandez-Diaz, R. Martinez-Coronado, L. P. Cao, X. Li, L. G. Marshall, C. Q. Jin, and J. B. Goodenough, Identification of electronic state in perovskite CaCrO$_3$ by high-pressure studies, Phys. Rev. B **92**, 144421 (2015).

[26] J. Zhao, N. L. Ross, and R. J. Angel, New view of the high-pressure behaviour of GdFeO$_3$-type perovskites, Acta Crystallogr., Sect. B **60**, 263 (2004).

[27] N. L. Ross and T. D. Chaplin, Compressibility of CaZrO$_3$ perovskite: Comparison with Ca-oxide perovskites, J. Solid State Chem. **172**, 123 (2003).

[28] N. L. Ross and R. J. Angel, Compression of CaTiO$_3$ and CaGeO$_3$ perovskites, Am. Mineral. **84**, 277 (1999).

[29] T. B. Ballaran, R. G. Trønnes, and D. J. Frost, Equations of state of CaIrO$_3$ perovskite and post-perovskite phases, Am. Miner. **92**, 1760 (2007).

[30] J. S. Zhou, Structural distortions in rare-earth transition-metal oxide perovskites under high pressure, Phys. Rev. B **101**, 224104 (2020).

[31] See Supplemental Material at http://link.aps.org/supplemental/10.1103/PhysRevB.108.134106 for the experimental details and more refinement results.

[32] Y. Fei, A. Ricolleau, M. Frank, K. Mibe, G. Shen, and V Prakapenka, Toward an internally consistent pressure scale, Proc. Natl. Acad. Sci. **104**, 9182 (2007).

[33] V. Petříček, M. Dušek, and L. Palatinus, Crystallographic Computing System JANA2006: General features, Z. für Kristall. - Crys. Mater. **229**, 345 (2014).

[34] F. Izumi and T. Ikeda, Mater. Sci. Forum **321-324**, 198 (2000).

[35] K. Momma and F. Izumi, VESTA 3 for three-dimensional visualization of crystal, volumetric and morphology data, J. Appl. Crystallogr. **44**, 1272 (2011).

[36] C. Prescher and V. B. Prakapenka, DIOPTAS: A program for reduction of two-dimensional X-ray diffraction data and data exploration, High Pressure Res. **35**, 223 (2015).

[37] J. Rodríguez-Carvajal, Recent advances in magnetic structure determination by neutron powder diffraction, Physica B **192**, 55 (1993).

[38] J. Prado-Gonjal, R. Schmidt, J.-J. Romero, D. Ávila, U. Amador, and E. Morán, Microwave-assisted synthesis, microstructure, and physical properties of rare-earth chromites, Inorg. Chem. **52**, 313 (2013).

[39] M. Marezio, J. P. Remeika, and P. D. Dernier, The crystal chemistry of the rare earth orthoferrites, Acta Crystallogr., Sect. B **26**, 2008 (1970).

[40] J. P. Wignacourt, J. S. Swinnea, H. Steinfink, and J. B. Goodenough, Oxygen atom thermal vibration anisotropy in $Ba_{0.87}K_{0.13}BiO_3$, Appl. Phys. Lett. **53**, 1753 (1988).

[41] H. Taguchi, Relationship between crystal structure and electrical properties of $Nd(Cr_{1-x}Fe_x)O_3$, J. Solid State Chem. **131**, 108 (1997).

[42] Y. G. Shi, Y. F. Guo, S. Yu, M. Arai, A. A. Belik, A. Sato, K. Yamaura, E. Takayama-Muromachi, H. F. Tian, H. X. Yang, J. Q. Li, T. Varga, J. F. Mitchell, and S. Okamoto, Continuous metal-insulator transition of the antiferromagnetic perovskite $NaOsO_3$, Phys. Rev. B **80**, 161104(R) (2009).

[43] S. Layek, E. Greenberg, S. Chariton, M. Bykov, E. Bykova, D. M. Trots, A. V. Kurnosov, I. Chuvashova, S. V. Ovsyannikov, I. Leonov, and G. K. Rozenberg, Verwey-type charge ordering and site-selective Mott transition in Fe_4O_5 under pressure, J. Am. Chem. Soc. **144**, 10259 (2022).

[44] Y. Zhang, S. Chariton, J. He, S. Fu, F. Xu, V. B. Prakapenka, and J.-F. Lin, Atomistic insight into the ferroelastic post-stishovite transition by high-pressure single-crystal X-ray diffraction, Am. Miner. **108**, 110 (2023).

[45] J. Ruiz-Fuertes, T. Bernert, D. Zimmer, N. Schrodt, M. Koch-Müller, B. Winkler, L. Bayarjargal, C. Popescu, S. MacLeod, and K. Glazyrin, Ambient-temperature high-pressure-induced ferroelectric phase transition in $CaMnTi_2O_6$, Phys. Rev. B **96**, 094101 (2017).

[46] J. S. Zhou and J. B. Goodenough, Universal octahedral-site distortion in orthorhombic perovskite oxides, Phys. Rev. Lett. **94**, 065501 (2005).

[47] S. Calder, V. O. Garlea, D. F. McMorrow, M. D. Lumsden, M. B. Stone, J. C. Lang, J. W. Kim, J. A. Schlueter, Y. G. Shi, K. Yamaura, Y. S. Sun, Y. Tsujimoto, and A. D. Christianson, Magnetically driven metal-insulator transition in $NaOsO_3$, Phys. Rev. Lett. **108**, 257209 (2012).

[48] R. H. Mitchell, *Perovskites: Modern and Ancient* (Almaz Press, Ontario, 2002).

[49] M. Amboage, M. Hanfland, J. A. Alonso, and M. J. Martínez-Lope, High pressure structural study of $SmNiO_3$, J. Phys.: Condens. Matter **17**, S783 (2005).

[50] T. Hashimoto, N. Matsushita, Y. Murakami, N. Kojima, K. Yoshida, H. Tagawa, M. Dokiya, and T. Kikegawa, Pressure-induced structural phase transition of $LaCrO_3$, Solid State Commun. **108**, 691 (1998).

[51] T. Shibasaki, T. Furuya, J. Kuwahara, Y. Takahashi, H. Takahashi, and T. Hashimoto, Exploration of high pressure phase in $LaGaO_3$ and $LaCrO_3$, J. Therm. Anal. Calorim. **81**, 575 (2005).

[52] B. J. Kennedy, T. Vogt, C. D. Martin, J. B. Parise, and J. A. Hriljac, Pressure-induced orthorhombic to rhombohedral phase transition in $LaGaO_3$, J. Phys.: Condens. Matter **13**, L925 (2001).

[53] R. J. Angel, J. Zhao, N. L. Ross, C. V. Jakeways, S. A. T. Redfern, and M. Berkowski, High-pressure structural evolution of a perovskite solid solution $(La_{1-x}, Nd_x)GaO_3$, J. Solid State Chem. **180**, 3408 (2007).

[54] M. Medarde, J. Mesot, S. Rosenkranz, P. Lacorre, W. Marshall, S. Klotz, J. S. Loveday, G. Hamel, S. Hull, and P. Radaelli, Pressure-induced orthorhombic-rhombohedral phase transition in $NdNiO_3$, Physica B **234-236**, 15 (1997).

[55] W. M. Xu, O. Naaman, G. K. Rozenberg, M. P. Pasternak, and R. D. Taylor, Pressure-induced breakdown of a correlated system: The progressive collapse of the Mott-Hubbard state in $RFeO_3$, Phys. Rev. B **64**, 094411 (2001).

[56] G. Kh. Rozenberg, M. P. Pasternak, W. M. Xu, L. S. Dubrovinsky, S. Carlson, and R. D. Taylor, Consequences of pressure-instigated spin crossover in $RFeO_3$ perovskites; a volume collapse with no symmetry modification, Europhys. Lett. **71**, 228 (2005).

[57] A. G. Gavriliuk, I. A. Troyan, R. Boehler, M. I. Eremets, I. S. Lyubutin, and N. R. Serebryanaya, Electronic and structural transitions in $NdFeO_3$ orthoferrite under high pressures, J. Exp. Theor. Phys. Lett. **77**, 619 (2003).

[58] J. S. Zhou and J. B. Goodenough, Intrinsic structural distortion in orthorhombic perovskite oxides, Phys. Rev. B **77**, 132104 (2008).

[59] P. M. Woodward, T. Vogt, D. E. Cox, A. Arulraj, C. N. R. Rao, P. Karen, and A. K. Cheetham, Influence of cation size on the structural features of $Ln_{1/2}A_{1/2}MnO_3$ perovskites at room temperature, Chem. Mater. **10**, 3652 (1998).

[60] M. O'Keeffe and B. G. Hyde, Some structures topologically related to cubic perovskite ($E2_1$), ReO_3 ($D0_9$) and Cu_3Au ($L1_2$), Acta Crystallogr., Sect. B **33**, 3802 (1977).

[61] O. L. Anderson and N. Soga, A restriction to the law of corresponding states, J. Geophys. Res. **72**, 5754 (1967).

[62] D. L. Anderson and O. L. Anderson, Brief report: The bulk modulus-volume relationship for oxides, J. Geophys. Res. **75**, 3494 (1970).

[63] Y. Zhao, D. J. Weidner, J. Ko, K. Leinenweber, X. Liu, B. Li, Y. Meng, R. E. G. Pacalo, M. T. Vaughan, Y. Wang, and A. Yeganeh-Haeri, Perovskite at high P-T conditions: An in situ synchrotron X ray diffraction study of $NaMgF_3$ perovskite, J. Geophys. Res.: Solid Earth **99**, 2871 (1994).

[64] N. L. Ross, J. Zhao, R. J. Angel, High-pressure structural behavior of GaO_3 and $GdFeO_3$ perovskites, J. Solid State Chem. **177**, 3768 (2004).

[65] J. Chen and J. S. Zhou (unpublished).

[66] D. Bloch, The 103 law for the volume dependence of superexchange, J. Phys. Chem. Solids **27**, 881 (1966).

[67] K. N. Shrivastava and V. Jaccarino, Variation of superexchange with interatomic distance. I. The T_{2g} system $V^{++}-F^--V^{++}$, Phys. Rev. B **13**, 299 (1976).

[68] J. R. Smith, Self-consistent many-electron theory of electron work functions and surface potential characteristics for selected metals, Phys. Rev. **181**, 522 (1969).

[69] J. He and C. Franchini, Screened hybrid functional applied to $3d^0 \rightarrow 3d^8$ transition-metal perovskites $LaMO_3$ ($M = $ Sc-Cu): Influence of the exchange mixing parameter on the structural, electronic, and magnetic properties, Phys. Rev. B **86**, 235117 (2012).

[70] K. J. May and A. M. Kolpak, Improved description of perovskite oxide crystal structure and electronic properties using self-consistent Hubbard U corrections from ACBN0, Phys. Rev. B **101**, 165117 (2020).

[71] H. J. Xiang, M. Guennou, J. Íñiguez, J. Kreisel, and L. Bellaiche, Rules and mechanisms governing octahedral tilts in perovskites under pressure, Phys. Rev. B **96**, 054102 (2017).

[72] Y. Zhang, J.-J. Gong, C.-F. Li, L. Lin, Z.-B. Yan, S. Dong, and J.-M. Liu, Strain-induced Slater transition in polar metal $LiOsO_3$, Phys. Status Solidi RRL **13**, 1900436 (2019).

[73] C. H. Kronbo, L. R. Jensen, F. Menescardi, D. Ceresoli, and M. Bremholm, High-pressure, low-temperature studies of phase transitions in $SrRuO_3$-Absence of volume collapse, J. Solid State Chem. **287**, 121360 (2020).

[74] S. Sasaki, C. T. Prewitt, J. D. Bass, and W. A. Schulze, Orthorhombic perovskite $CaTiO_3$ and $CdTiO_3$: Structure and space group, Acta Crystallogr., Sect. C **43**, 1668 (1987).

[75] I. Levin, T. G. Amos, S. M. Bell, L. Farber, T. A. Vanderah, R. S. Roth, and B. H. Toby, Phase equilibria, crystal structures, and dielectric anomaly in the $BaZrO_3$-$CaZrO_3$ system, J. Solid State Chem. **175**, 170 (2003).

[76] S. Sasaki, C. T. Prewitt, and R. C. Liebermann, The crystal structure of $CaGeO_3$ perovskite and the crystal chemistry of the $GdFeO_3$-type perovskites, Am. Miner. **68**, 1189 (1983).

[77] A. Vegas, M. Vallet-Regi, J. M. Gonzalez-Calbet, and M. A. Alario-Franco, The $ASnO_3$ ($A =$ Ca, Sr) perovskites, Acta Crystallogr., Sect. B **42**, 167 (1986).

[78] J.-I. Yamaura, S. Yonezawa, Y. Muraoka, and Z. Hiroi, Crystal structure of the pyrochlore oxide superconductor KOs_2O_6, J. Solid State Chem. **179**, 336 (2006).

[79] N. E. Brese and M. O'Keeffe, Bond-valence parameters for solids, Acta Crystallogr., Sect. B **47**, 192 (1991).

[80] J. Zhao, N. L. Ross, D. Wang, and R. J. Angel, High-pressure crystal structure of elastically isotropic $CaTiO_3$ perovskite under hydrostatic and non-hydrostatic conditions, J. Phys.: Condens. Matter **23**, 455401 (2011).

[81] J. Zhao, N. L. Ross, and R. J. Angel, Tilting and distortion of $CaSnO_3$ perovskite to 7 GPa determined from single-crystal X-ray diffraction, Phys. Chem. Miner. **31**, 299 (2004).